

# Micro-mechanism of Fracture Failure of Fissured Rock Mass under Uniaxial Compression Based on PFC2D

Zhichen Yang, Jiajun Zeng\*, Qiyun Wang, Qingqing Shen, Qiang Zeng

**Abstract**—The morphology of primary fractures significantly influences the strength and failure characteristics of rock masses. To elucidate the meso-scale fracture mechanisms in fissured rock masses during uniaxial compression failure, specimens with varying dip angles were prefabricated for uniaxial compression testing. This study investigates the mechanical characteristics and crack evolution models of rock mass specimens influenced by different fracture dip angles. In addition, by combining particle flow numerical simulation, the distribution of particle displacement field in the fissured rock mass during loading was explored, revealing the evolution of force chains around the pre-existing fissures.

**Index Terms**—Fissured rock mass, Mechanical characteristics, Particle displacement field, Force chain field, Fracture mechanism

## I. INTRODUCTION

After a prolonged geological process, natural rock mass will develop discontinuities such as joints, fractures, weak planes, and faults of varying sizes and shapes [1-4]. These discontinuities can generate new, propagating discontinuities under the action of external loads. Furthermore, they can weaken the rock's mechanical properties and influence the initiation, propagation, and failure patterns of cracks within the rock under load. The formation of cracks in a single-fissure rock-like specimen during uniaxial compression is depicted in Fig. 1 [3]. Two common types of cracks (wing cracks and secondary cracks [5-7]) typically develop at the tips of prefabricated fissures. An airfoil crack represents a type of tensile crack that

initiates near the tip of a prefabricated fissure and extends steadily in alignment with the direction of maximum compressive stress. Secondary cracking occurs later in the process but spreads rapidly; it often serves as a primary cause for the failure observed in fissured rock-like specimens. Secondary cracks can be categorized into two types: secondary coplanar cracks and secondary inclined cracks. A secondary coplanar crack is characterized as a shear crack that originates at the tip of a prefabricated fissure while propagating approximately within the same plane. Conversely, a secondary inclined crack develops at an angle to the pre-existing fissure (similar to wing cracks) but propagates in the opposite direction; this type is also known as an anti-wing crack. The failure mechanisms associated with rock masses are frequently linked to the initiation, propagation, and interconnection among diverse types of fractures. Therefore, it is essential to investigate both the evolution mechanisms and mechanical response characteristics related to rock mass fractures under loading conditions.

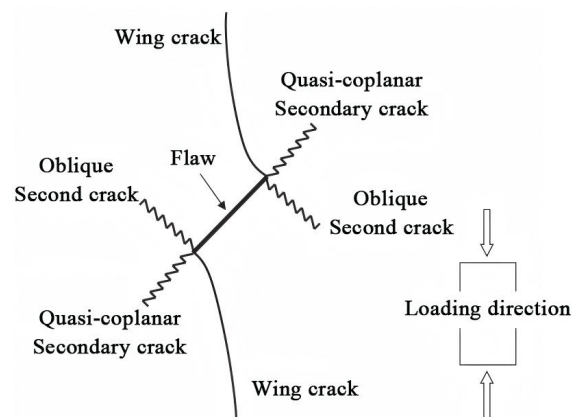


Fig. 1. Schematic diagram of the cracking mode

Researchers typically utilize real rock or materials with analogous properties (such as cement, gypsum, glass, and 3D printing materials) to fabricate various forms of rock samples containing a single discontinuity through cutting or prefabrication. They then conduct uniaxial compression tests to investigate the mechanisms of crack initiation and propagation, as well as the mechanical properties and failure mechanisms of rock masses influenced by different discontinuities [8-18]. Since 2020, Liu et al. have performed uniaxial compression tests on rock materials featuring a single fracture to examine the evolution characteristics of full-field strain under varying stress levels [19]. Shen et al.

Manuscript received April 24, 2024; revised January 3, 2024. This work was supported in part by the Natural Science Foundation of Hunan Province (2023JJ50104); Scientific Research Fund of Hunan Provincial Education Department (22B0853, 23B0838, 24A0659, 24B0840), Hunan Institute of Technology provincial-level applied characteristic discipline (KFB23022), National College Student Innovation and Entrepreneurship Training Program Project (S202311528042).

Zhichen Yang is an Undergraduate at College of civil and construction engineering, Hunan Institute of Technology, Hengyang 421002, China (e-mail: 1214176464@qq.com).

Jiajun Zeng is a Lecturer at College of civil and construction engineering, Hunan Institute of Technology, Hengyang 421002, China (corresponding author to provide phone: +86-186-0733-4330; e-mail: zengjiajun93@163.com).

Qiyun Wang is a Professor at College of civil and construction engineering, Hunan Institute of Technology, Hengyang 421002, China (e-mail: wangqiyun860519@163.com).

Qingqing Shen is a Lecturer at College of civil and construction engineering, Hunan Institute of Technology, Hengyang 421002, China (e-mail: 1039095517@qq.com).

Qiang Zeng is a Lecturer at College of civil and construction engineering, Hunan Institute of Technology, Hengyang 421002, China (e-mail: 405973504@qq.com).

explored the behavior of crack initiation and propagation in single-crack rock materials affected by different crack widths [20]. Xin et al., employing numerical image correlation techniques, analyzed the strain field evolution mechanism in sandstone subjected to uniaxial compression [21]. Xu et al. investigated the crack evolution and macroscopic failure modes in joint Phyllite under uniaxial compression [22]. Yuan et al. utilized both uniaxial compression tests and particle flow program (PFC2D) simulations to assess how crack inclination influences mechanical properties, crack propagation, and failure modes in red sandstone [23]. Wei et al. employed ultrasonic testing, uniaxial compression tests, conventional triaxial compression methods, Brazilian splitting techniques, X-ray diffraction analysis, scanning electron microscopy among other approaches to evaluate the physical and mechanical properties of four groups of samples with varying water content while studying gypsum rock's physical and mechanical characteristics [24].

The rapid and convenient numerical method has become a widely adopted approach for investigating the deformation and failure mechanisms of rock materials [25]. In recent years, research utilizing numerical simulations based on PFC2D/3D has gradually gained prominence, offering a more realistic and reliable representation of the fracture behavior of rock materials compared to other numerical simulation techniques. Numerous researchers have employed PFC2D/3D to examine the mechanical characteristics associated with fracture failure in fissured rock masses, as well as crack initiation and propagation. Liu et al. established a PFC2D numerical model for a single fissured rock mass, analyzing its mechanical behavior, failure process, and microscopic displacement patterns under uniaxial compression [26]. Zhang et al. developed a similar single fissured rock mass model using PFC2D to investigate both fracture behavior and acoustic emission characteristics during uniaxial compression [27]. Yao et al. explored the uniaxial compressive strength, failure modes, micro-crack initiation processes, and displacement behaviors within rock mass models subjected to numerical simulations of uniaxial compression [28]. Zhao et al. utilized PFC3D to simulate three-dimensional brittle rock materials featuring open internal fracture structures while examining their fracture failure characteristics under uniaxial compression [29]. Chen et al. integrated mechanical data from laboratory tests on rock mass materials to construct a three-dimensional fracture numerical model aimed at studying the influence of joint dip angle on mechanical behavior, fracturing processes, and displacement fields within the rock mass [30].

Although numerous indoor experiments and numerical simulations have been conducted on fissured rock masses, existing research has primarily concentrated on the mechanical characteristics of these materials and the macroscopic evolution mechanisms of cracks. However, the evolution mechanisms governing the displacement field and force chain field of microparticles in proximity to prefabricated cracks remain poorly understood. It is essential to begin with an exploration and description of microscopic characteristics, thereby delving into both micro- and macro-mechanisms that contribute to the

complex macroscopic behaviors observed in fractured rock materials. Consequently, this article presents findings from indoor uniaxial compression tests on fissured rock masses, complemented by numerical simulations using the discrete element program PFC2D. The study investigates peak strength characteristics of fissured rock mass, crack evolution mechanisms, particle displacement field characteristics at crack initiation, as well as distribution patterns within the force chain field during loading processes. The results provide valuable insights for subsequent research focused on understanding the meso-fracture mechanisms inherent in fissured rock masses.

## II. EXPERIMENTAL OVERVIEW

### A. Sample preparation

The rock-like materials utilized in this test are prepared by mixing white cement, fine sand, and water in a mass ratio of 5:5:2, specifically using 425 white cement. Prior to the preparation of the test specimen, an embedded steel sheet must be inserted into the designated hole of the mold. This steel sheet is subsequently removed after the initial setting of the specimen to create a prefabricated crack. The formwork should be dismantled 24 hours post-pouring of the test piece, and any qualified specimens shall then be placed in a curing box for a duration of 28 days.

A schematic diagram illustrating the crack specimen is presented in Figure 2. The overall dimension of the test piece is 200mm × 150mm × 50mm, the crack length is  $2a = 30\text{mm}$ , and the crack opening  $b$  is 0.8mm respectively. The angle of the prefabricated crack is the included angle between the prefabricated crack and the horizontal axis. The gradient of the prefabricated crack is  $15^\circ$  ( $\beta = 0^\circ, 15^\circ, 30^\circ, 45^\circ, 60^\circ, 75^\circ$  and  $90^\circ$ ).

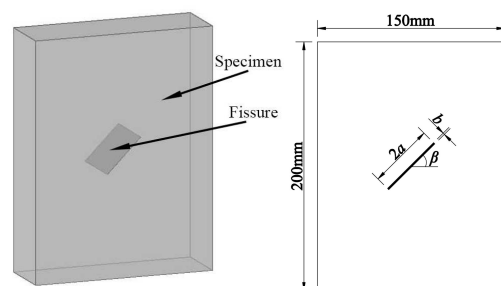


Fig.2. Specimen model and thickness of the steel sheet

### B. Physical test situation

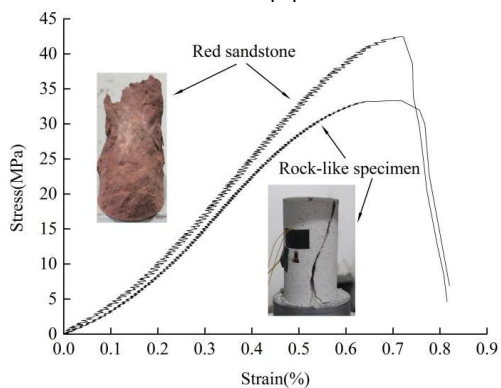
The RMT-150B rock mechanics testing machine was employed for the loading tests. The loading mode utilized in this experiment is force control, with a loading speed of 200 N/s. Throughout the loading process, an HD digital camera recorded the entire procedure, capturing images of the specimen's final failure mode.

Under identical test conditions, uniaxial compression tests, Brazilian splitting tests, and direct shear tests were conducted on complete specimens prepared from cement mortar. The physical and mechanical parameters of these rock-like materials are summarized in Table 1. Figure 3(b) illustrates the stress-strain relationship curve and compares the failure modes of intact rock specimens with those of red sandstone specimens under uniaxial loading. The results

presented in this figure indicate that both types exhibit three distinct deformation stages on their stress-strain curves: initial compaction, elastic deformation, and plastic yield. Notably, compared to red sandstone specimens, the initial compaction and plastic yield stages of the stress-strain curve for rock-like specimens are prolonged due to a higher presence of defects such as microvoids within the cement mortar matrix. Overall, it can be concluded that the mechanical properties and characteristics of stress-strain curves for these prepared rock-like materials closely align with those observed in actual red sandstone.



(a) RMT-150B rock mechanics test equipment



(b) Comparison chart of test results

Fig. 3. Test system and test result diagram

Table I Mechanical parameters of rock-like materials and red sandstone

Variable name (unit)	Symbol	Value (Specimens)	Value (Red sandstone)
Density(kg/m <sup>3</sup> )	$\rho$	2145	2258
Peak strength(MPa)	$\sigma_{max}$	33.28	42.43
Elastic modulus(GPa)	$E_c$	7.63	8.26
Poisson ratio	$\nu$	0.21	0.20
Tensile strength(MPa)	$\sigma_t$	2.64	2.79
Cohesion(MPa)	$c$	6.49	7.14
Friction angle(°)	$\varphi$	33.75	34.68

C. Overview of Numerical Simulation

In this study, the uniaxial compression of the fracture model is simulated using the particle flow code PFC2D. The particle flow program encompasses two fundamental models: contact bonding and parallel bonding. The latter offers a more accurate representation of cementation between particles, providing resistance not only to tensile and shear forces but also to torque resulting from particle rotation or shear, as illustrated in Figure 4 [30].

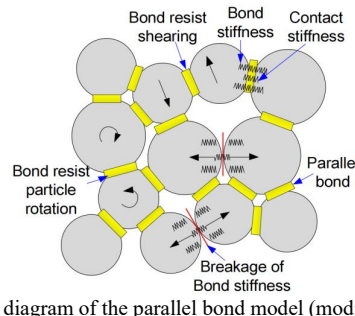


Fig. 4. Schematic diagram of the parallel bond model (modified from Chen et.al [30])

Therefore, this study employs the parallel bonding model for numerical simulations. A two-dimensional numerical model is developed using PFC2D. The stress-strain curve, peak strength, elastic modulus, and failure mode obtained from laboratory tests are selected as target variables for parameter calibration [26]. The numerical model is depicted in Figure 5.

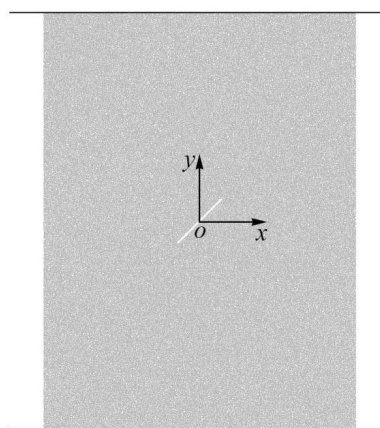


Fig. 5. Numerical model

The total number of particles in the complete numerical model is 44,285. Figure 6 illustrates the comparison between the results of the numerical simulation and those obtained from indoor tests. The stress-strain curve of the complete specimen exhibits three distinct deformation stages: initial compaction, elastic deformation, and plastic yield. Notably, both the initial compaction and plastic yield stages are prolonged due to numerous defects such as microvoids present in the cement mortar rock specimen. In contrast, the upward section of the numerical simulation curve increases approximately linearly. The peak strength of the complete numerical model is measured at 33.10 MPa, with an elastic modulus of 7.49 GPa. The failure mode observed aligns closely with that recorded in experimental tests, indicating that under these micromechanical parameters, the numerical model effectively reflects the macroscopic mechanical properties of rock mass as demonstrated in testing. The micromechanical parameters utilized within this numerical model are detailed in Table 2.

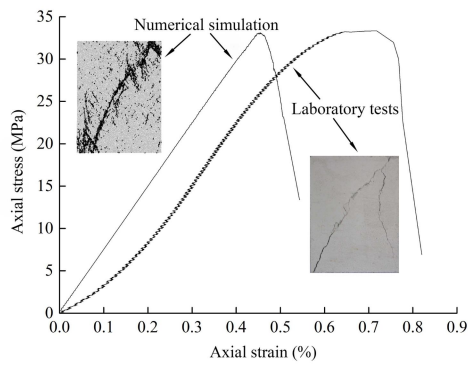


Fig. 6. Test results comparison

Table II Microscopic parameters of the numerical model

Variable name (unit)	Symbol	Value
Minimum radius of particles (mm)	$r_{min}$	0.7
Maximum radius of particles (mm)	$r_{max}$	1.05
Density of particle (kg/m <sup>3</sup> )	$\rho$	2150
Ball-ball contact modulus(GPa)	$E$	4.5
Normal-to-shear stiffness ratio of particle	$k_{ball}$	2.5
Friction coefficient of particles	$\mu$	0.4
Tensile strength of parallel bond (MPa)	$\sigma_{bond}$	14.5
Shear strength of parallel bond (MPa)	$\tau_{bond}$	15.5

### III. EXPERIMENTAL RESULTS

#### A. Analysis of mechanical characteristics

In the laboratory tests, the data acquisition system employed in the testing apparatus records both the load and compression deformation of cracked specimens during loading. The acquired test data are subsequently processed. Figure 7 illustrates the axial stress-strain curves obtained from both laboratory tests and numerical simulations. During uniaxial compression, fractured rock samples undergo three distinct stages of deformation: initial compaction, elastic deformation, and plastic yield. Notably, the stress-strain curves for rock samples with varying fracture dip angles exhibit similar characteristics. In the numerical simulation, it is observed that the stress-strain curve increases linearly prior to reaching its peak value.

The relationship curve depicting the peak stress of fissured rock mass specimens influenced by fracture inclination is illustrated in Figure 8 (a). As shown in this figure, the peak strength of the fissured rock mass observed in both laboratory tests and numerical simulations reaches a minimum at an inclination angle of 0° and a maximum at 90°. The trend regarding the variation of peak strength with increasing fracture inclination is consistent across both laboratory tests and numerical simulations, demonstrating an upward trajectory as the fracture inclination increases. Notably, at any given inclination angle, the peak strength derived from numerical simulations exceeds that obtained from indoor testing.

Figure 8 (b) presents the variation curve for the elastic modulus of fractured rock mass under experimental testing conditions compared to those predicted by numerical models. With an increase in crack inclination angle, both indoor experiments and numerical simulations exhibit a rising trend in elastic modulus. However, it is noteworthy that fluctuations in elastic modulus values are relatively minor within numerical simulations, whereas significant variability is observed within indoor experimental results.

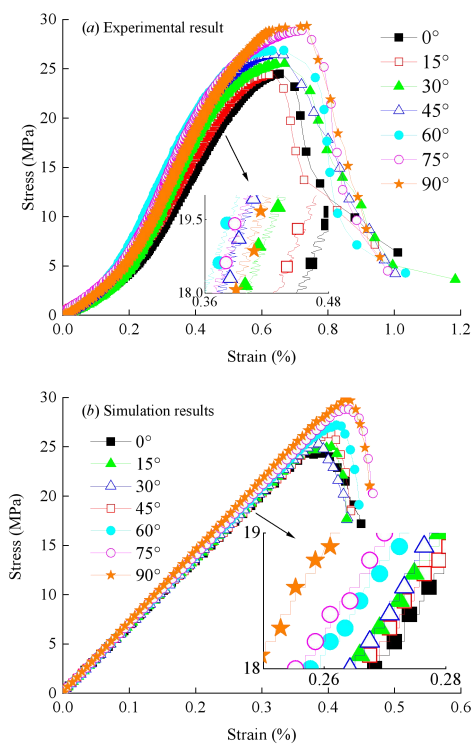


Fig. 7. Comparison of stress-strain curves of fissured rock mass

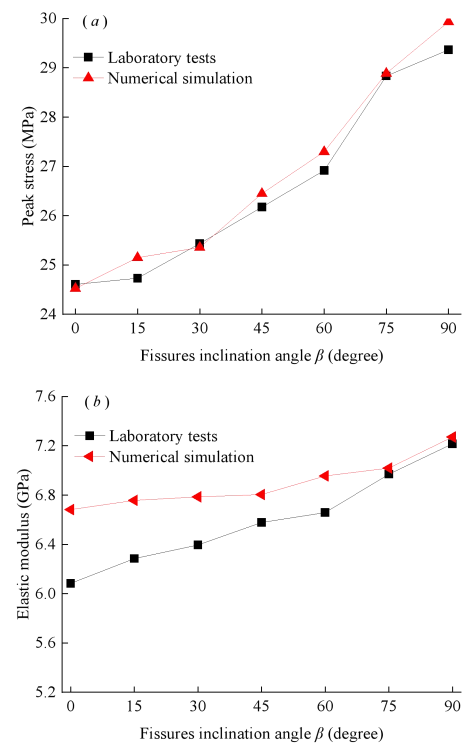


Fig.8. Peak stress and elastic modulus change curve

#### B. Analysis of crack evolution characteristics

##### (1) Crack initiation mode

During the loading process, the entire procedure was documented using a high-definition digital camera. Following the test, the recorded video was analyzed frame by frame to identify the crack initiation modes of specimens with varying degrees of opening. In the numerical simulation, Fish language was employed to capture the apparent morphology of the fracture model at specific time steps. Figure 9 illustrates both laboratory tests and numerical simulations regarding crack initiation modes in fractured

rock masses.

When the crack dip angle is  $0^\circ$ , cracking initiates near the center of the prefabricated crack, manifesting as a tensile crack that propagates along the direction of maximum principal stress. At dip angles of  $15^\circ$ ,  $30^\circ$ ,  $45^\circ$ , and  $60^\circ$ , crack initiation occurs at the tip of the prefabricated crack; these are classified as wing cracks extending toward areas of maximum compressive stress. As we approach a dip angle of  $75^\circ$ , signs of crack initiation at this tip become less pronounced; here, wing cracks initiated from this point exhibit delayed formation and shorter propagation paths.

At an inclination angle of  $90^\circ$ , laboratory tests reveal a tensile crack propagating in alignment with that same prefabricated structure at its upper tip, while no cracking is observed at its lower tip. In contrast, numerical simulations indicate numerous microcracks dispersed across the surface of specimens modeled with a  $90^\circ$  inclination.

In the numerical simulation, three primary types of displacement fields are identified [31]: type I displacement field under tensile fracture, type III displacement field under tensile shear mixed fracture, and type II displacement field under shear fracture, as illustrated in Fig. 10. Through numerical simulations, we observe the displacement characteristics of particles on the flaw surface and analyze the crack initiation mechanism from a microscopic perspective. When the crack in the numerical model initiates, the meso-particle displacement field surrounding the initial crack is depicted in Figure 11.

From the particle displacement field on the fracture surface (Fig. 11), it can be observed that when the fracture inclination is at  $0^\circ$ , a type I displacement field resulting from tensile fracture emerges near the center of the prefabricated fracture surface. The direction of these displacement vectors is shown in Fig. 9a, elucidating the micro-mechanism underlying tensile cracking at this central location; as for cracks with dip angles of  $15^\circ$ ,  $30^\circ$ ,  $45^\circ$ , and  $60^\circ$ , wing cracks develop at their tips. Analysis of particle displacements reveals that an I-type particle displacement field manifests at these tips upon crack initiation, indicating that wing cracks arise due to relative tensile stress.

When examining a crack dip angle of  $75^\circ$ , we find that a type I particle displacement field appears at lower tip during initial cracking while both type I and type II particle displacement fields emerge simultaneously at upper tip. This suggests that cracking initiated at this upper tip results not solely from tensile stress but rather from a combined effect of both tensile and shear stresses.

### (2) Failure mode analysis

The final failure mode of the fractured specimen is illustrated in Figure 12. The failure modes of crack specimens with varying dip angles are characterized by shear cracks that initiate at the tip of the prefabricated crack, subsequently overlapping and penetrating both the upper and lower loading surfaces of the specimen. Notably, the failure modes observed under these two working conditions closely resemble those of  $90^\circ$  crack specimens and intact specimens.

In contrast, under other working conditions, the shear crack within the fissured rock mass specimen originates from both tips of the prefabricated crack. This shear crack rapidly extends towards both upper and lower interfaces of

the specimen, ultimately merging with the prefabricated crack to create a macro shear fracture surface. This process culminates in an instability failure.

### (3) Force-chain

In order to further investigate the development and evolution of cracks near the prefabricated crack surface, we tracked and recorded the distribution characteristics of force chains during both crack initiation and propagation in a numerical simulation of the crack model specimen. Throughout the loading process, the specimen underwent four distinct stages: initial compression, initial crack initiation, secondary crack initiation and propagation, and ultimate specimen failure. These stages are denoted as "stage 1," "stage 2," "stage 3," and "stage 4," respectively. Figure 13 illustrates the force chain distribution for fracture models with varying dip angles across these four stages. The particles are obscured in this figure; however, it is important to note that the red lines represent microcracks generated during loading, while green and black lines denote tensile force chains and compression force chains of parallel bonds, respectively. Furthermore, the thickness of each force chain line indicates the magnitude of resultant forces acting on parallel bonds, whereas its direction reflects that of contact resultant forces. The generation of microcracks in Discrete Element Method (DEM) simulations is characterized by parallel breaking among particles connected by bonds. Consequently, variations in defect distributions throughout this process—specifically regarding both size and directional forces—serve to illustrate to some extent how forces evolve around defects.

Figure 14 presents a simplified diagram illustrating the evolution process of the force chain field in the vicinity of prefabricated cracks at various loading stages and dip angles. By examining Figures 13 and 14 together, it is evident that during the initial compression stage (Stage 1), concentrated areas of the compression force chain (denoted as black area A) emerge at both left and right edges of the prefabricated cracks, while concentrated areas of the tensile force chain (indicated as green area B) develop at the top and bottom. This observation indicates that stress concentration occurs in regions a and b. Notably, both the location and size of these concentration areas for compression force chains (black area A) and tensile force chains (green area B) remain relatively stable despite variations in crack opening.

At a consistent dip angle, during crack initiation and propagation, there is a transfer of concentrated tensile force chains towards the crack tip, leading to a gradual dissipation of the tensile force chain field surrounding the prefabricated crack. As the dip angle increases, tensile force chains on either side of the prefabricated crack shift from central positions toward both ends; this behavior reflects changes in crack initiation positioning while simultaneously resulting in diminishing sizes for concentrated areas associated with tensile forces. Concurrently, there is a reduction in both concentration areas for tensile forces as well as driving forces for wing crack initiation—this aligns with observations indicating an increase in time required for crack initiation corresponding to higher dip angles. Following wing crack initiation, there is an accelerated dissipation rate observed within concentrated areas of tensioned force chains; additionally, it has been noted that

wing cracks exhibit progressively shorter lengths over time.

IV. CONCLUSION

This article systematically investigates the micro-mechanical mechanisms underlying rock mass fracture failure influenced by crack inclination angles. The following conclusions are drawn: (1) As the inclination angle of the fissure increases, both the peak strength and elastic modulus of the fissured rock mass exhibit a gradual increase. Additionally, the initial position of crack initiation shifts from near the center of the prefabricated fissure to its tip. (2) A concentration area for compressive force chains emerges

at the tip of the prefabricated crack, while areas for tensile force chain concentration appear at both ends (top and bottom) of this crack. With crack initiation and propagation, these tensile force chain concentration areas migrate with the advancing crack tip and gradually dissipate. (3) During the initial compression stage, as the dip angle of the prefabricated crack increases, there is a transfer in tensile force chain concentration from mid-crack to both ends. Furthermore, this concentration area diminishes progressively over time. This phenomenon elucidates changes in both crack initiation position and timing.



Fig. 9. Crack initiation mode

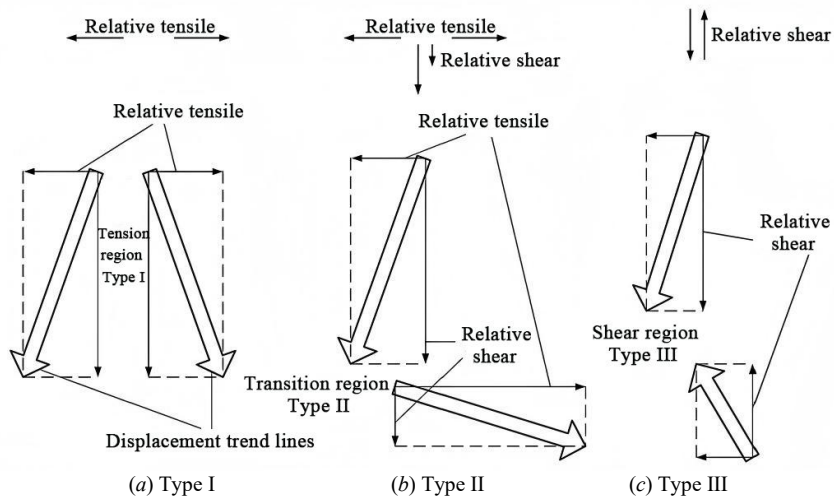


Fig. 10. Three types of displacement fields, as defined by the displacement vector

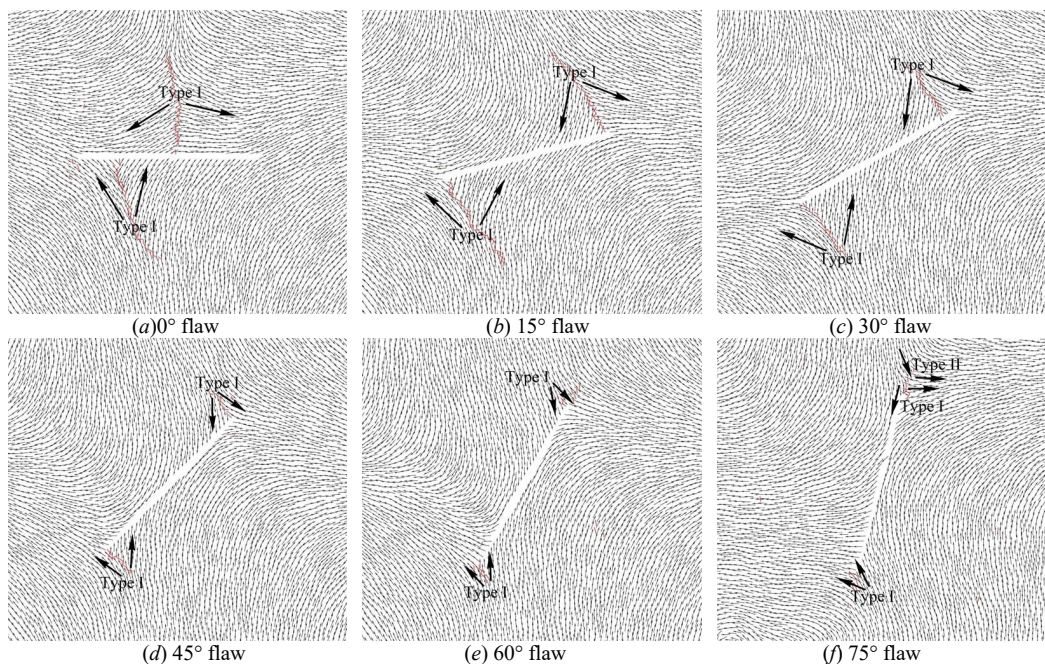


Fig. 11. Crack initiation mode and the surface displacement field of the flaw

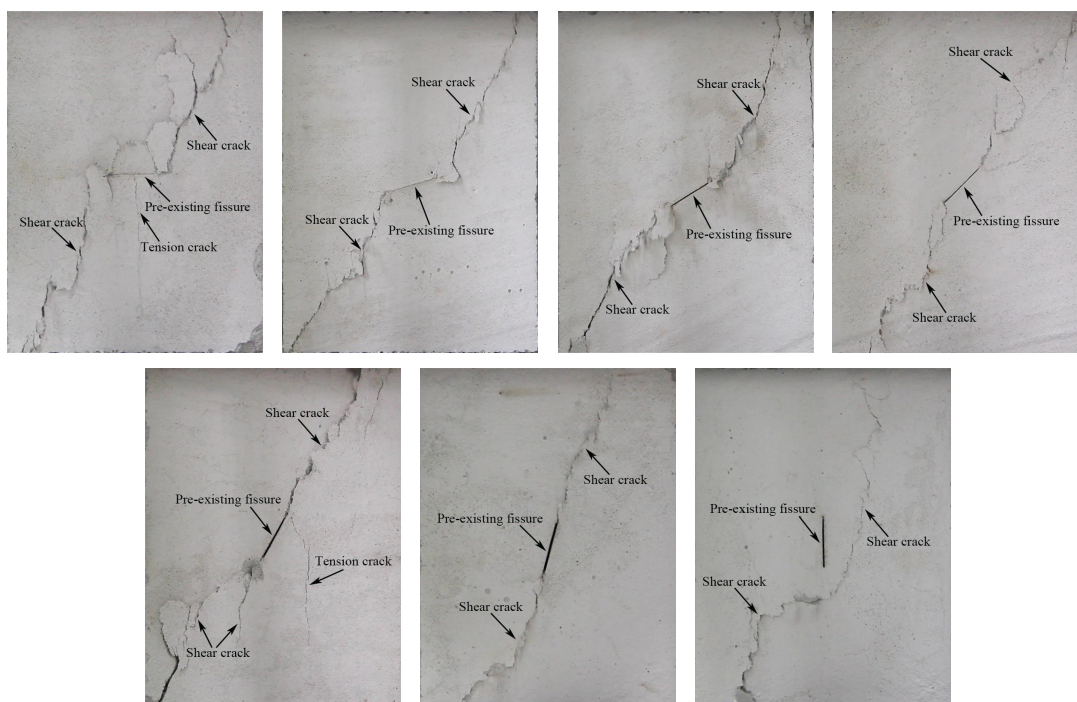


Fig. 12. Failure mode of fissure rock-like specimens

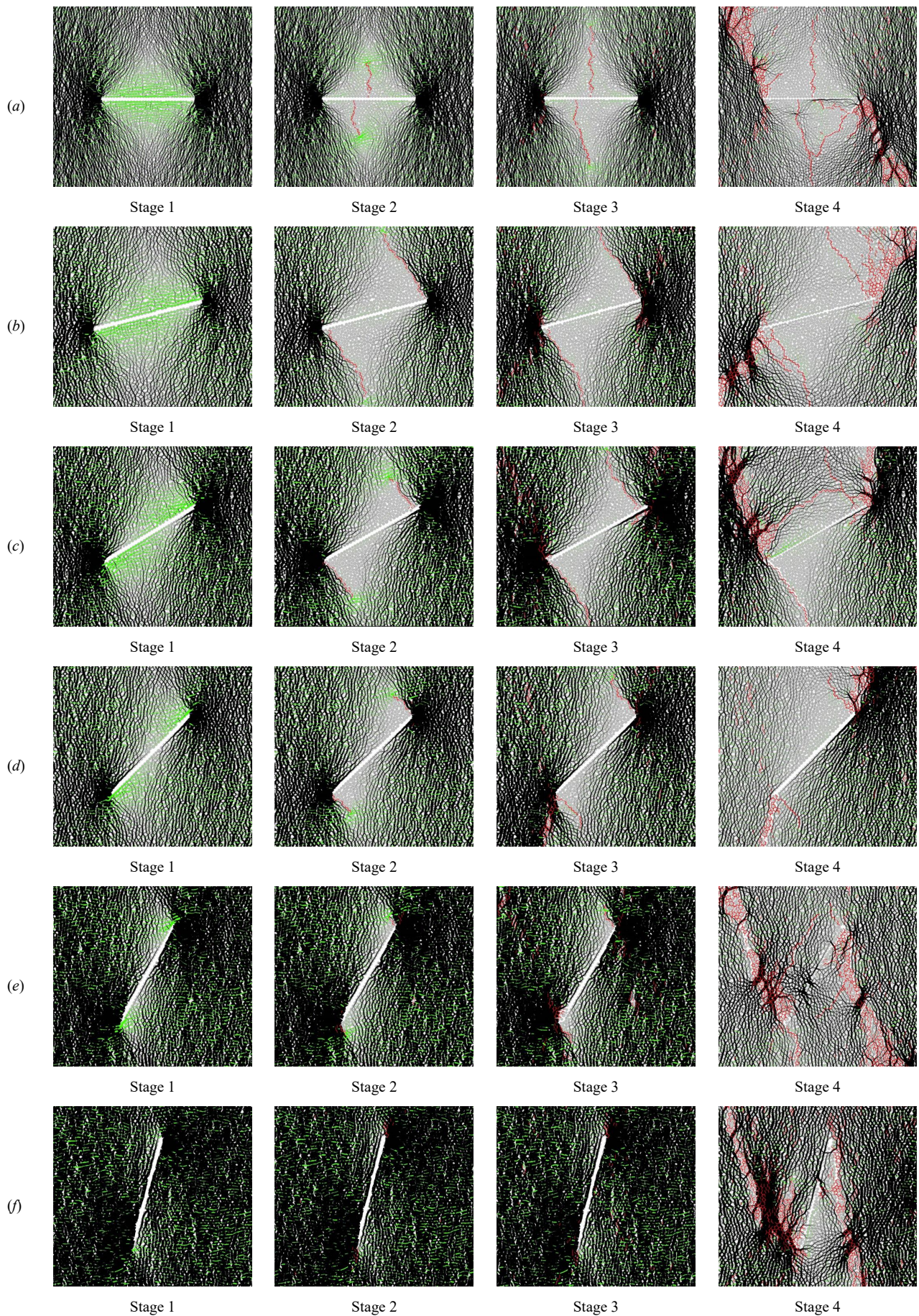


Fig.13 Distribution of the force-chain field around the flaw at four stages under the different fissure apertures (a)  $0^\circ$ , (b)  $15^\circ$ , (c)  $30^\circ$ , (d)  $45^\circ$ , (e)  $60^\circ$  and (f)  $75^\circ$  (green lines indicate the tensile force-chain, black lines indicate the compressive force-chain, and red lines indicate the ruptured parallel bonds). (For interpretation of the references to color in this figure legend, the reader is referred to the web version of this article.)

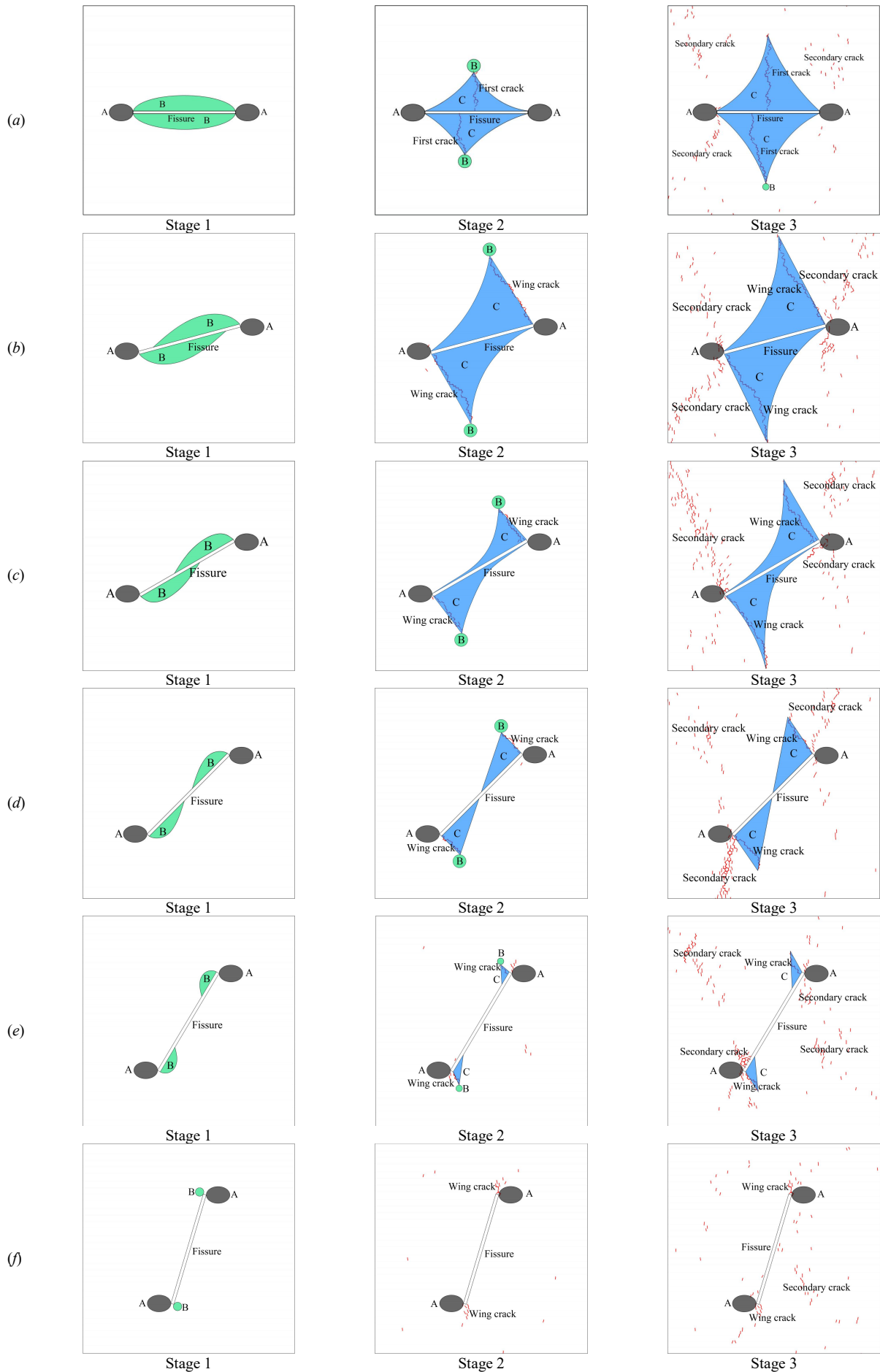


Fig. 14 Distribution evolution of the strong force-chain field around the fissure at different loading stages when the fissure apertures are (a)  $0^\circ$ , (b)  $15^\circ$ , (c)  $30^\circ$ , (d)  $45^\circ$ , (e)  $60^\circ$  and (f)  $75^\circ$  (black regions A indicate the concentration regions of the strong compressive force-chain, green regions B indicate the concentration regions of the strong tensile force-chain, and blue regions C indicate the “force-chain dissipation region”).

REFERENCES

- [1] Bobet, A., Einstein, H. H., Fracture coalescence in rock-type material under uniaxial and biaxial compression. *International Journal of Rock Mechanics and Mining Sciences*, vol. 35, no. 7, pp. 863-888, 1998.
- [2] Cao, P., Liu, T., Pu, C. and Lin, H., Crack propagation and coalescence of brittle rock-like specimens with pre-existing cracks in compression. *Engineering Geology*, vol. 187, pp. 113-121, 2015.
- [3] Cao, R.H., Cao, P., Lin, H., Ma, G.W., Fan, X. and Xiong, X.G., Mechanical behavior of an openings in a jointed rock-like specimen under uniaxial loading: Experimental studies and particle mechanics approach. *Archives of Civil and Mechanical Engineering*. vol. 18, no. 1, 198-214, 2018.
- [4] Yang S Q, Tian W L, Huang Y H, et al, Experimental and discrete element modeling on cracking behavior of sandstone containing a single oval flaw under uniaxial compression. *Engineering Fracture Mechanics*, vol. 194, pp. 154-174, 2018.
- [5] Wong, R.H.C., Chau, K.T., Tang, C.A., Lin, P., Analysis of crack coalescence in rock-like materials containing three flaws—part I: experimental approach. *Int. J. Rock Mech. Min. Sci.* vol. 38, pp. 909–924 2001.
- [6] Park, C.H., Bobet, A., Crack coalescence in specimens with open and closed flaws: a comparison. *Int. J. Rock Mech. Min. Sci.* vol. 46, no. 5, pp. 819–829, 2009.
- [7] Camones, L.A.M., Vargas, E.d.A., de Figueiredo, R.P. and Velloso, R.Q., Application of the discrete element method for modeling of rock crack propagation and coalescence in the step-path failure mechanism. *Engineering Geology*, vol. 153, pp. 80-94, 2013.
- [8] Bobet A, Einstein HH. Fracture coalescence in rock-type materials under uniaxial and biaxial compression. *Int. J. Rock Mech Min Sci Geomech Abs*, vol. 35, no. 7, pp. 863–88, 2013.
- [9] Li Y, Chen L, Wang Y. Experimental research on pre-cracked marble under compression. *Int J Solids Struct*, vol. 42, no. 9, pp.2505–2516, 2005.
- [10] Park CH, Bobet A. Crack coalescence in specimens with open and closed fl-flaws: a comparison. *Int J Rock Mech Min Sci*, vol. 46, no. 5, pp. 819–829, 2009.
- [11] Sheng-Qi Y, Hong-Wen J. Strength failure and crack coalescence behavior of brittle sandstone samples containing a single fissure under uniaxial compression. *Int J Fract*, vol. 168, no. 2, pp. 227–250, 2011.
- [12] Xu T, Ranjith P G, Wasantha P L P, et al. Influence of the geometry of partially-spanning joints on mechanical properties of rock in uniaxial compression. *Engineering Geology*, vol. 167, no. 24, pp. 134-147, 2013.
- [13] Zhuang X, Chun J, Zhu H. A comparative study on unfilled and filled crack propagation for rock-like brittle material. *Theoretical & Applied Fracture Mechanics*, vol. 72, no. 1, pp. 110-120, 2014.
- [14] Ha, Y. D., Lee, J. and Hong, J. W.. Fracturing patterns of rock-like materials in compression captured with peridynamics. *Engineering Fracture Mechanics*, vol. 144, pp. 176-193, 2015.
- [15] Liu T. , Lin B. , Yang W. , et al. Cracking Process and Stress Field Evolution in Specimen Containing Combined Flaw Under Uniaxial Compression. *Rock Mechanics & Rock Engineering*, vol. 49, no. 8, pp. 3095-3113, 2016.
- [16] Ma, G.W., Dong, Q.Q., Fan, L.F. and Gao, J.W.. An investigation of non-straight fissures cracking under uniaxial compression. *Engineering Fracture Mechanics*, vol. 191, pp. 300-310, 2018.
- [17] Wang Y, Tang J, Dai Z, et al. Experimental study on mechanical properties and failure modes of low-strength rock samples containing different fissures under uniaxial compression. *Engineering Fracture Mechanics*, vol. 197, pp. 1-20, 2018.
- [18] Wang Y, Tang J, Dai Z, et al. Experimental study on mechanical properties and failure modes of low-strength rock samples containing different fissures under uniaxial compression. *Engineering Fracture Mechanics*, vol. 197, pp.1-20, 2018.
- [19] Liu, Liwang, Li, Haibo, Li, Xiaofeng, Wu, Renjie. Full-field strain evolution and characteristic stress levels of rocks containing a single pre-existing flaw under uniaxial compression. *Bulletin of Engineering Geology and the Environment*, vol. 79, pp. 3145-3161, 2020.
- [20] Shen J , Zhan S , Karakus M , et al. Effects of flaw width on cracking behavior of single-flawed rock specimens. *Bulletin of Engineering Geology and the Environment*, vol. 80, no. 2, pp. 1701-1711, 2020.
- [21] Xin, C., Yang, Y., Yang, M. et al. Study on Strain Field Evolution of Uniaxial Compression Sandstone Based on Digital Image Correlation Technology. *Appl. Sci*, vol. 12, no. 11939, 2022.
- [22] Xu, J., Fei, D., Yu, Y. et al. Research on crack evolution law and macroscopic failure mode of joint Phyllite under uniaxial compression, *Sci Rep*, vol. 11, no. 419, 2021.
- [23] Yue Yuan, Jinlei Fu, Xiaolei Wang, Xi Shang, "Experimental Study on Mechanical Properties of Prefabricated Single-Cracked Red Sandstone under Uniaxial Compression", *Advances in Civil Engineering*, vol. 2020, no. 8845368, 2020.
- [24] Sijiang Wei, Chongyang Wang, Yushun Yang, Meng Wang, "Physical and Mechanical Properties of Gypsum-Like Rock Materials", *Advances in Civil Engineering*, vol. 2020, no. 3703706, 2020.
- [25] Jin J., P. Cao, Y. Chen, et al. Influence of single flaw on the failure process and energy mechanics of rock-like material, *Computers and Geotechnics*, vol. 86, pp.150-162, 2017.
- [26] Liu T, Lin B, Zou Q, et al. Mechanical behaviors and failure processes of precracked specimens under uniaxial compression: A perspective from microscopic displacement patterns, *Tectonophysics*, vol. 672, pp. 104-120, 2016.
- [27] Zhang X P, Zhang Q, Wu S. Acoustic emission characteristics of the rock-like material containing a single flaw under different compressive loading rates. *Computers & Geotechnics*, vol. 83, pp. 83-97, 2017.
- [28] Yao, N.; Ye, Y.C.; Hu, B.; Wang, W.Q.; Wang, Q.H. Particle flow code modeling of the mechanical behavior of layered rock under uniaxial compression. *Arch. Min. Sci.* vol. 64, pp.181-196, 2019.
- [29] Zhao, Y., Gao, Y. & Wu, S. Experimental and Numerical Studies of Brittle Rock-Like Samples with Internal Open Fractures and Cavities Under Uniaxial Compression. *Arab J Sci Eng*, vol. 45, pp. 8349–8368, 2020.
- [30] M. Chen, SQ. Yang, P. Gamage Ranjith, Y-C. Zhang, Cracking behavior of rock containing non-persistent joints with various joints inclinations, *Theoretical and Applied Fracture Mechanics*, vol. 109, no. 102701, 2020.
- [31] Zhang X P, Liu Q, Wu S, et al. Crack coalescence between two non-parallel flaws in rock-like material under uniaxial compression[J]. *Engineering Geology*, vol. 199, pp. 74-90, 2015.